

MODEL PREDICTION FOR AN OBSERVED FILAMENT

G. AULANIER

Naval Research Laboratory, Code 7675A, Washington, DC 20375; aulanier@godzilla.nrl.navy.mil

N. SRIVASTAVA

Max-Planck-Institut für Aeronomie, D-37191 Katlenburg-Lindau, Germany

AND

S. F. MARTIN

Helio Research, 5212 Maryland Avenue, La Crescenta, CA 91214

Received 2000 March 10; accepted 2000 June 12

ABSTRACT

This paper presents the results of a “blind test” for modeling the structure of an observed filament using the three-dimensional magnetohydrostatic model recently developed by Aulanier et al. in 1999. The model uses a constant shear α , and it takes into account the effects of pressure and gravity. The test consisted of predicting the structure of a filament (observed in the southern hemisphere) with a minimum observational input: only a line-of-sight magnetogram, with a straight line drawn on it to show the location of the filament, was provided. The filament was chosen by the observers (N. S. and S. F. M.) because it had a definite overall left-handed structural pattern known as sinistral, but the direction of component of the magnetic field along the filament axis was uncertain from the combination of $H\alpha$ data and magnetograms. The modeler (G. A.) evaluated and fixed the values of some of the free parameters of the model while some others were varied in reasonable ranges. The $H\alpha$ image of the filament was revealed only after the modeling. For $\alpha > 0$, the three-dimensional distribution of magnetic dips computed by the model fairly well reproduces the structure of the filament and its barbs. Moreover, the models for which $\alpha < 0$ do not match well the observations. This study then shows the first successful theoretical prediction for the magnetic field of an observed filament. It shows that the method based on the Aulanier et al. model is a powerful tool, not only for purposes of modeling, but also for prediction of the chirality, helicity, and morphology of observed filaments.

Subject headings: MHD — Sun: filaments — Sun: magnetic fields — Sun: prominences

1. INTRODUCTION

The magnetic configuration of filaments has been a long puzzle since the early years of solar physics (see the review of Tandberg-Hanssen 1998), in particular concerning the problem of mass support in such high structures (10–100 Mm) in which the pressure scale height is so small (200–500 km). Observations of plasma flows in filaments and prominences show typical velocities of the order of 1–10 km s⁻¹ in their feet and 10–30 km s⁻¹ in their main body (see, e.g., Malherbe et al. 1983; Schmieder 1990; Athay 1990; Schmieder, Raadu, & Wiik 1991; Zirker, Martin, & Engvold 1998; Wang 1999). The motions in the body of prominences are mainly horizontal, which is in agreement with magnetic measurements of prominence fields done with the Hanle effect (see the review of Bommier 1998), which show horizontal fields. The orientation of the flows in the feet is still under debate: Aulanier et al. (1999) suggested that projection effects may lead to confusions because horizontal fields may appear vertical on the line of sight. The observed velocities are much smaller than the free-fall, sound, and Alfvén speeds.

These combined results have been used in models which imply that the plasma can be considered to be in vertical equilibrium and that most of the observed flows are probably pressure-driven flows that are aligned with a magnetic field which evolves quasi-statically. Several competing mechanisms have been proposed to hold the dense prominence plasma against gravity. One example is the damping of Alfvén waves in vertical fields (Jenssen 1990), but this process suffers from many difficulties (Engvold 1998).

Another idea is that slow magnetic reconnection near the photosphere can lift mass into the corona at the sites of canceling magnetic fields in filament channels (Martin 1992; Priest 1998; Litvinenko & Martin 1999), but all details of this mechanism are not yet worked out. Until now, most theorists and some observers believe that the tension of dipped magnetic field lines can provide a magnetic support (see the review of Démoulin 1998). Cold plasma is believed to be formed and trapped in such “magnetic dips” (Antiochos & Klimchuk 1991 and references therein).

A large number of models for prominences based on magnetic dips have been deeply investigated. In two-dimensions (or 2.5D), the models have thus far considered three classes of configurations: simple arcades, in which the plasma bends the field and produces dips (e.g., Kippenhahn & Schlüter 1957; Wu et al. 1990; Fiedler & Hood 1993); quadrupolar regions, in which the dips are naturally present above the X-point (e.g., Kippenhahn & Schlüter 1957; Uchida 1981, 1998; Malherbe & Priest 1983; Amari & Aly 1992; Démoulin & Priest 1993; Cheng & Choe 1998); and finally twisted flux ropes, in which dips are present below the O-point (Kuperus & Raadu 1974; Priest, Hood, & Anzer 1989; van Ballegoijen & Martens 1989; Démoulin & Priest 1989, 1992; Inhester, Birn, & Hesse 1992; Amari & Aly 1992; Rust & Kumar 1994; Low 1994). The development of three-dimensional models is very recent. However, because of computational limits, they have seldom been compared with observations. Three-dimensional models generally have been inspired from the previous two-dimensional works, i.e., quadrupolar fields (Galsgaard &

Longbottom 1999), twisted flux ropes with less than one turn (Antiochos, Dahlburg, & Klimchuk 1994), and those with more than one turn (van Ballegooijen 1999; Amari et al. 1999; DeVore & Antiochos 2000).

In the past few years, the first comparisons of some of these models with observations have been done. In this context, Filippov (1995), Low & Hundhausen (1995), and Aulanier & Démoulin (1998) have shown that the twisted flux tube models are able to reproduce the typical orientations of fibrils generally observed in filament channels (Martin, Bilimoria, & Tracadas 1994). Also, the three-dimensional flux rope model of Aulanier & Démoulin (1998) naturally reproduced the observed lateral extensions of filaments known as feet or “barbs.” This model also reproduced the observed chirality patterns for the barbs, as well as their relation with some “parasitic polarities” observed in filament channels (Martin 1990, 1998; Martin et al. 1994). Parasitic polarities are defined by small areas of magnetic field opposite in polarity to the dominant polarity of the network magnetic fields on one side of a filament or filament channel (i.e., in a region where $B_z < 0$ dominates, a parasitic polarity has $B_z > 0$).

Following this finding, Aulanier et al. (1998) proposed a linear force-free field model for an observed filament. The photospheric magnetogram was there modeled as a series of theoretical magnetic sources to represent the observed polarities in the “filament channel.” The filament channel was there defined as the region around the neutral line where the field is highly sheared. The main body of the filament was formed by a twisted flux rope (with less than one turn) in a bipolar region. The parasitic polarities near the neutral line led to a local perturbation of the magnetic fields in the corona, which led to the formation of lateral dips that appeared aside from the flux rope. These dips have been related to observed barbs. A sketch of the resulting magnetic field geometry can be found in Kucera et al. (1999). We would like to mention that Forbes (1997) was the first to propose a two-dimensional model where a barb was associated to a parasitic polarity located at the edge of a flux rope. His configuration was in fact very similar to the one derived in Aulanier et al. (1998). However, he interpreted the barb as a group of arcades going into the parasitic polarity and not as the distribution of dips. Finally, note that MacKay, Longbottom, & Priest (1999) confirmed the results of Aulanier et al. (1998), reproducing the formation of dips by parasitic polarities on the side of a weakly twisted flux rope but doing so with a different numerical method.

The model has been developed further in Aulanier et al. (1999), so that it can now (1) take the observed photospheric magnetogram from the filament channel as boundary conditions and (2) take into account some simplified form for the effects of plasma pressure and of solar gravity (using the solutions derived by Low 1992). Performing direct comparisons with observations, the model has been applied successfully to the evolution of an intermediate filament during one day (Aulanier et al. 1999) and to the fine structures of the barb of an active-region filament (A. A. van Ballegooijen et al., 2000, in preparation).

This paper reports a “blind test” we performed to check the robustness of the Aulanier et al. (1999) model. In the blind test, the parameters could not be fine-tuned to optimize the comparison with $H\alpha$ observations because the latter were not provided to the modeler! In other words, we tested how well the model can predict the structure of observed filaments using only a magnetogram. Section 2

describes the conditions under which the test was performed and what reasons motivated two of us (N. S. and S. F. M.) to choose the filament on which the model was applied. Note that the collaboration between the three authors in this paper was particularly interesting as two of us (N. S. and S. F. M.) wish to remain neutral observers and do not endorse the hypotheses on which all theoretical models are based at this time, including the one used here (see Martin 1998 and Zirker et al. 1998 for discussions on some observational constraints). In § 3, we describe the magnetic field reconstruction method and what is particular for the filament model. In § 4, we describe how the values for the free parameters were chosen. In § 5, assuming that the computed magnetic dips are a good tracer of $H\alpha$ absorbing material, we compare the filament morphology predicted by the model with the filament observed in $H\alpha$. In § 6, we discuss a possible reason for the orientation of barbs with respect to the spine of the filament, and we discuss the capability of the model to find the chirality and the helicity in observed filaments. We summarize the results of the blind test in § 7, and we conclude on the robustness of the model for prediction purposes.

2. INPUTS FOR THE “BLIND TEST”

This section first describes what kinds of filaments are most suitable for testing the Aulanier et al. (1999) model, especially with reference to the one that was chosen for the present study. Further, we list the limited inputs that were provided for the purpose of modeling.

2.1. Choice of the Filament

The limitations inherent to the Aulanier et al. (1999) model require that the portion of a filament to be modeled has a nearly straight body (or spine). This does not forbid the study of horseshoe-shaped filaments, as long as the filament is roughly straight in the region of interest (as in A. A. van Ballegooijen et al., 2000, in preparation). Several parts of one given horseshoe-shaped filament can then be modeled independently. Moreover, as the model uses observed magnetograms as boundary conditions, the selected filament needs to be not too far from the disk center. Gary & Hagyard (1990) and Démoulin et al. (1997) have shown that magnetic extrapolations are still reliable for a region located at 40° off the disk center, so that one can consider this as a good limit.

Keeping in view the above constraints, two of us (N. S. and S. F. M.) chose two candidate filaments. The preferred one was an ideal quiescent filament with distinct structure positioned among network magnetic fields of low flux density. The other filament was intermediate between a quiescent and active-region filament. The alternative was given because the network flux density around the ideal filament was so low that near the filament it was not clear which network polarity was dominant out to a distance of 100 Mm from either side of the filament. The one selected by the modeler (knowing only the magnetic field circumstance) was the quiescent filament, which was the greater challenge to the model given the low density of the network.

The filament was the northern section of a horseshoe-shaped filament located at E34S17 on 1999 November 4. From the observer’s perspective, it was chosen for several reasons: (1) it had several very long lateral extensions, or barbs, extending out of its spine and connecting in the sur-

rounding chromosphere; (2) the chirality of the filament was known (it was sinistral although it possessed one anomalous barb not fitting the overall sinistral pattern); and (3) the network magnetic field on the two sides of the filament was so weak that the dominant polarities did not stand out from the mixed polarity background of intranetwork and ephemeral region fields. Hence, the direction of the magnetic field along the axis of the filament was uncertain.

The filament was observed in $H\alpha$ at the Big Bear Solar Observatory (BBSO) and at Helio Research, as part of the Joint Observing Campaign (JOP 114) with the *Solar and Heliospheric Observatory (SOHO)* (conducted by N. S.). The full-disk BBSO $H\alpha$ image was recorded with a 20 cm aperture telescope. A partial frame is shown in Figure 1a. Note that this image was not revealed to the modeler (G. A.) until the calculations were done.

2.2. Line-of-Sight Magnetogram as Input

The only observational input provided for modeling was a medium-resolution full-disk magnetogram obtained at the Vacuum Telescope of the National Solar Observatory of the United States (NSO/KP), with a spatial resolution of $2''3$ (i.e., 1.66 Mm). Only the location of the filament was marked on the magnetogram by a straight line. The magnetogram coaligned with the $H\alpha$ image is shown on Figure 1b.

This provided the following information: (1) the detailed distribution of photospheric line-of-sight fields in the filament channel and its surroundings, which was later used as boundary conditions for the model; (2) the ability to calculate the precise location of the large-scale polarity inversion line (the so-called neutral line) on which the filament was lying, which otherwise would have been hard to identify because of the weak background bipolar magnetic field; and (3) the knowledge of which hemisphere on the Sun the filament belonged to.

From this information, and extending the results of Seehafer (1990), Pevtsov, Canfield, & Metcalf (1995), and Can-

field & Pevtsov (1998) on active regions and sunspots to filaments and filament channels, the modeler assumed that the net helicity of the studied filament channel should be positive. This comes from the fact that the Aulanier & Démoulin (1998) model (as well as every other model based on flux ropes—see § 1) calculates the helicity of the majority filaments in the southern hemisphere to be positive. Note that this result differs from the “wire model,” based on purely morphological deductions, described by Martin & McAllister (1997), which suggests that the helicity of most of the filaments of the southern hemisphere is negative. A discussion about this controversial result is provided in DeVore & Antiochos (2000).

3. THE THREE-DIMENSIONAL FILAMENT MODEL

In this section, we first describe the equations used for reconstructing three-dimensional magnetic fields in the corona using the observed photospheric magnetogram as a boundary condition. Then, we describe the model assumptions specific to the modeling of filaments.

3.1. Extrapolation Method

Under specific conditions (such as in uniform gravity), Low (1992) has shown that the combination of the equations governing a magnetohydrostatic field, i.e.:

$$\mathbf{j} \times \mathbf{B} - \nabla p + \rho \mathbf{g} = 0 . \quad (1)$$

$$\nabla \cdot \mathbf{B} = 0 , \quad (2)$$

$$\nabla \times \mathbf{B} = \mu \mathbf{j} , \quad (3)$$

could be rewritten as follows.

$$\nabla \times \mathbf{B} = \mathbf{j}(\text{force-free}) + \mathbf{j}(\text{plasma}) . \quad (4)$$

In Cartesian coordinates, where (x, y) is the photospheric plane, z is the altitude in the corona, and $\mathbf{u}_{x, y, z}$ are the unit

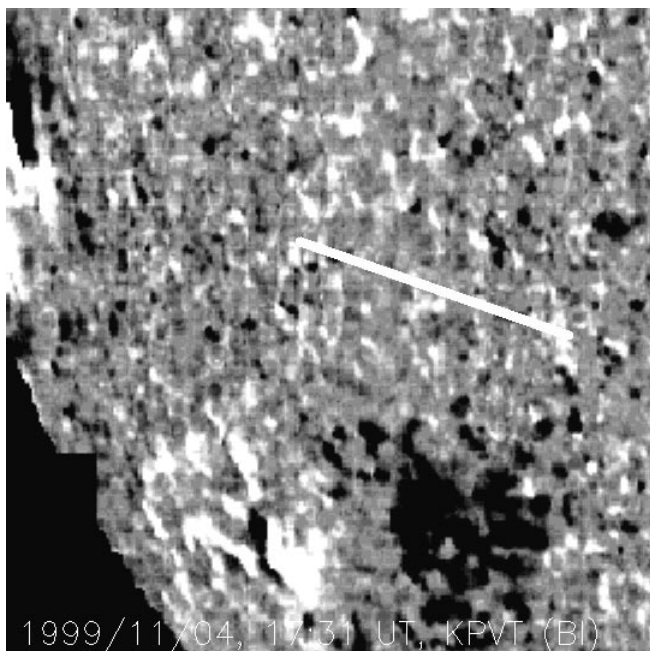


FIG. 1a

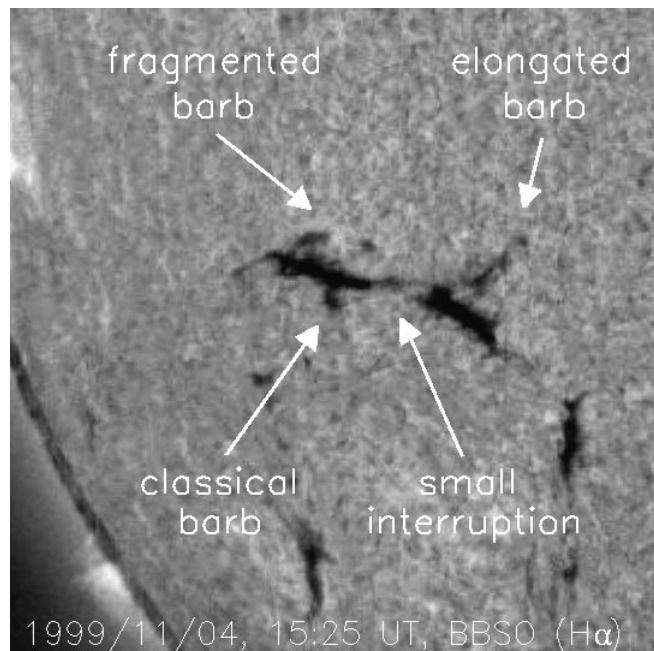


FIG. 1b

FIG. 1.— (a) Line-of-sight medium-resolution magnetogram obtained by Kitt Peak Vacuum Telescope (17:31 UT). (b) Big Bear $H\alpha$ image (15:25 UT). Both images are coaligned. Location of the filament (E34S17) is shown by the thick white line on the magnetogram.

vectors, the two terms for the currents in equation (4) are

$$\mathbf{j}(\text{force-free}) = \alpha \mathbf{B}, \quad (5)$$

$$\mathbf{j}(\text{plasma}) = a \exp(-z/H) \nabla B_z \times \mathbf{u}_z. \quad (6)$$

The first term here (eq. [5]) corresponds to the currents of a force-free field (in the absence of pressure and gravity), which are always aligned with the magnetic field. The second term (eq. [6]) describes the cross-fields currents that are always parallel to the photosphere and are induced by the gravity and the plasma pressure. α is the force-free field parameter and is always constant along field lines; however, it can differ from one field line to another. H is the scale height of the plasma effects, so that the field gradually passes from a non-force-free state near the photosphere to a nearly force-free state in the corona. Finally, a is a measure of the strength of the plasma effects. For a constant value of α , Low (1992) has derived analytical solutions for equation (4). By analogy with the linear force-free field for which $\mathbf{j}(\text{plasma}) = 0$, these solutions were named as the “linear magnetohydrostatics” (*lmhs*) equations.

The model developed by Aulanier et al. (1999) relies on magnetic field extrapolations in Cartesian coordinates, using the solutions of Low (1992). First, the observed magnetogram $B_z(x, y, z = 0)$ is decomposed in Fourier harmonics. So the method uses periodic boundary conditions in (x, y) . Second, assuming that the magnetic field drops to zero at infinite heights, the two other components (B_x, B_y) are calculated at $z = 0$, and then the three components of the field are computed for subsequent z . The computation method is then the same as the one used by Alissandrakis (1981) and Démoulin (1998) for linear force-free fields. Consequently, the same limitations on the force-free parameter apply to this method, i.e., one must keep

$$\alpha < \alpha(\text{res}) = 2\pi/L, \quad (7)$$

where L is the size of the periodicity of the field in the (x, y) directions and $\alpha(\text{res})$ is the resonant value above which harmonics with infinite energy in the field start to appear.

3.2. Assumptions for Modeling Filaments

The extrapolation method described in § 3.1 can be applied to model the three-dimensional magnetic configuration of many solar phenomena. In the case of filaments, we assume that the filament material observed in absorption in $H\alpha$ is the tracer of the dipped portions of upward curved field lines. The magnetic dips are numerically computed using the criterion given in Aulanier & Démoulin (1998):

$$B_x \frac{\partial B_z}{\partial x} + B_y \frac{\partial B_z}{\partial y} > 0, \quad (8)$$

only where $B_z = 0$. We then assume that the plasma can be observed on a pressure scale height in each computed magnetic dip, from their bottom to a height d . The model does not explain how the dense plasma can be injected into the dip. Antiochos & Klimchuk (1991), Dahlburg, Antiochos, & Klimchuk (1998), and Antiochos et al. (1999) have shown that a cold condensation can form in a preexisting magnetic dip. Whether this injection process occurs on the Sun or not, it is assumed that the plasma sits in every computed dip.

Filippov (1995), Low & Hundhausen (1995), and Aulanier & Démoulin (1998) have shown that twisted flux ropes

embedded in bipolar regions are good candidates for the magnetic configuration in filaments. The presence of such twisted flux ropes requires a high value for the force-free field parameter α . Equation (7) shows that the model is limited in the sense that it cannot create strongly sheared regions embedded in less sheared (or potential) arcades, as observed by Schmieder et al. (1996) and used in many of the other three-dimensional models mentioned in § 1. However, it has been shown that this limitation was not a constraint as long as only the filament channel is modeled (see Aulanier et al. 1999 and A. A. van Ballegoijen et al., 2000, in preparation).

In some cases, the flux rope naturally appears from the extrapolations (A. A. van Ballegoijen et al., 2000, in preparation), but in other cases, in particular when the filament lies in a quiet Sun region for which the bipolar background is dispersed, the observed magnetogram needs to be modified on its sides in order to impose a background field that is favorable for the presence of such a flux rope when high shears are imposed (Aulanier et al. 1999). This procedure is described in the next section.

4. CHOICE OF THE PARAMETERS

This section details the procedure which permits to fix the parameters of the model. This procedure relies on the analysis of the large scale magnetogram, combined with its potential extrapolation. The choice of some parameters is also done under typical physical considerations for filaments in general.

4.1. The Free Parameters of the Model

In addition to the magnetogram $B_z(x, y, z = 0)$, there are 10 parameters in the present model:

d : the height of the dips on which the plasma is visible in absorption in $H\alpha$;

a : the strength of the plasma effects;

H : the scale height on which they decrease in altitude;

$\tilde{B}(i;0)$: the normalized values for the three harmonics for the twisted flux tube;

L : the width of the region of interest of the magnetogram;

δL : the width of the region not replaced by the harmonics;

f : a multiplicative factor for the amplitude of the harmonics; and

α : the force-free field parameter.

Since the plasma parameters cannot be fine-tuned by comparing the models with the observations, and as previous studies have shown that their effect only leads to a perturbation of the resulting force-free configuration (for which $a = 0$), $a = 1$ and $H = 10$ Mm are chosen. The filling height of the dips is assumed to be equal to the pressure scale height in filaments, so $d = 300$ km is chosen. These values are the same as in Aulanier et al. (1999).

4.2. Setting the Photospheric Boundary Conditions

A critical issue regarding the reconstruction of the magnetic field is to know which area (L^2) of the magnetogram given in § 2.2 needs to be considered for the extrapolations. In order to do so, the large-scale bipolar background field forming the filament channel needs to be identified.

Averaging the fields given by the magnetogram shown in Figure 1a revealed that the magnetic field to the south of the marked neutral line (NL) is dominated by negative flux, mainly coming from the leading polarity of the southern

active region. Moreover, the northern part is dominated by the dispersed positive network fields. A potential extrapolation (i.e., $\alpha = a = 0$) was done on the same area as the one shown in Figure 1a. The magnetogram was included in a larger region in which the field was set to be $B = 0$ to minimize the periodicity effects. A sharp gradient of connectivity was found (namely, a quasi-separatrix layer or QSL—see Démoulin et al. 1997) in the negative polarity of the active region: on one side of the QSL, the field lines connect to the positive polarity of the same active region, while on the other side they are connected to the northern network fields. The average distance from the NL to the QSL (≈ 133 Mm) is then taken as the half-width of the region to consider for modeling the filament channel only. The region of interest, for $L = 266$ Mm, is shown on Figure 2 (*left-hand panel*). We estimate an error of $\Delta L \approx \pm 20$ Mm.

As mentioned in § 3.2, the region of interest in the magnetogram needs to be modified to ensure the presence of a twisted flux rope. Following the same procedure as in Aulanier et al. (1999), we crop the magnetogram on its side: two strips on each side of the NL of a width of $0.2L$ are removed, in which the field is set to be $B_z = 0$. This is done to remove the dispersed large-scale bipolar component of the field while keeping the observed polarities in the central part of the region corresponding to a width $\delta L = 0.6L = 160$ Mm. To this cropped magnetogram is then added a 2.5D bipolar component (invariant by translation along the NL axis) formed by analytical harmonics. This is done in order to replace the observed dispersed bipolar component with a more homogeneous one.

For a prediction, the three harmonics cannot be determined from the magnetogram or by comparison with the H α observation. Any combination of three harmonics which ensures the presence of a twisted flux rope, in a bipolar magnetic field region for a high value of α , is supposed to be acceptable. This corresponds to the bipolar section of the “OX” and “OBP” regions shown on the Figures 1 and 2 of Aulanier & Démoulin (1998). For consistency with previous studies, the same values as in Aulanier et al. (1999) are chosen for the three harmonics.

4.3. The Multiplicative Parameter f

The amplitude of the harmonics are normalized values, which need to be multiplied by a factor f to correspond to magnetic fields in gauss. The choice for f is critical, as it measures the flux of the replaced homogeneous bipolar background.

The parameter f can be chosen such that the imposed background field has the same flux as the observed dispersed fields. In Aulanier et al. (1999), the choice for f was fine-tuned until the model got the best agreement with the H α image, but this procedure cannot be done for prediction purposes. In the present study, $f \approx 3.6$ is evaluated from the flux of the dispersed bipolar component for $L = 266$ Mm.

This estimate is subject to several uncertainties, first because it strongly depends on the size L of the region considered in the magnetogram. This effect on the value of f was tested by considering different values for L in the range of $L \pm \Delta L$. The resulting values for f are in the range of $f \approx 3.6 \pm 1$. The confidence in the precise value of f found above is also limited because the 2.5D harmonics replacing the dispersed fields lead to an artificial modification of the distribution of magnetic flux. Based on the results obtained in Aulanier et al. (1999), it is believed that the latter effect leads to a small overestimation of f .

Consequently, the precise value of f cannot be fixed, but for the present study, it can be varied in an estimated reasonable range of $2 < f < 4$. Figure 2 (*right-hand panel*) shows an example of a modified magnetogram that can be used in the calculations for the harmonics amplitudes given in § 4.2 with the mean value of $f = 3$.

4.4. On the Force-free Parameter α

Contrary to what one would expect, choosing the amplitude of $|\alpha|$ is not very difficult. As long as it is kept above its critical value $|\alpha|(\text{crit})$, above which a flux rope is present, a vertically extended twisted flux rope is obtained.

Choosing α closer and closer to its resonant value leads to a higher and higher filament, but this parameter cannot be adjusted as the H α image was not provided until the test

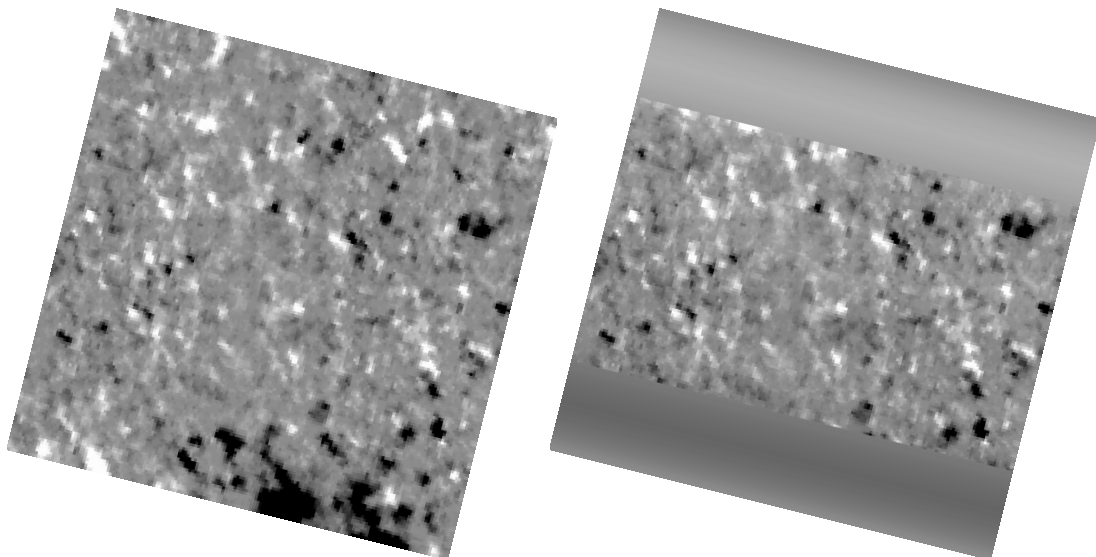


FIG. 2.— (*Left-hand panel*) Selected area of the NSO/KP magnetogram. The evaluation of its width $L = 266$ Mm is discussed in the text. (*Right-hand panel*) Modified magnetogram to be used in the linear magnetohydrostatics extrapolations. The modification procedure is described in the text. The harmonics used are listed in Table 1, and here $f = 3$.

model was completed. Note that for the harmonics chosen in § 4.2, $|\alpha|(\text{crit})/\alpha(\text{res}) \simeq 0.988$ (see Aulanier et al. 1999).

As $|\alpha|(\text{crit}) < |\alpha| < |\alpha|(\text{res})$ must be used, only small variations in α can be done. This implies that the field in the vicinity of the parasitic polarities will be weakly affected by these changes. This is because they can be decomposed in high-order Fourier harmonics, which are weakly affected by small variations of α (see Aulanier & Démoulin 1998). In other words, the modeled barbs do not highly depend on the precise value of α for the reconstruction method chosen here, although future models of filament barbs (such as with nonconstant α) could obtain different results.

Finally, $|\alpha|/\alpha(\text{res}) = 0.99$ was chosen, which gives a physical value of $|\alpha| = 2.3 \times 10^{-2} \text{ Mm}^{-1}$. It is worth noticing that this value is much smaller than for the observed intermediate and active-region filaments modeled in Aulanier et al. (1999) and A. A. van Ballegooijen et al. (2000, in preparation), for which $|\alpha| = 5.0 \times 10^{-2} \text{ Mm}^{-1}$ and $|\alpha| = 8.9 \times 10^{-2} \text{ Mm}^{-1}$, respectively. This is simply caused by the fact that L is much larger here than in the previous studies, while $|\alpha|/\alpha(\text{res})$ are of the same order.

To put constraints on the choice of the sign of α , the results of Seehafer (1990), Pevtsov, Canfield, & Metcalf (1995), and Canfield & Pevtsov (1998), based on active regions, are here extended to filaments. This leads to the inference that the magnetic field in the filament modeled in this study had an 80% or greater probability of having positive helicity as it is lying in the southern hemisphere. Hence, $|\alpha|/\alpha(\text{res}) = +0.99 > 0$ is chosen for the calculations.

5. RECONSTRUCTION OF THE MAGNETIC FIELD

This section describes the numerical computation of the dips for three models which use the parameters given in Table 1. We discuss the model predictions, and we then compare the three-dimensional distribution of dips with the H α observation of the filament.

5.1. Numerical Computation

The magnetic field extrapolations are performed from modified magnetograms (the right-hand panel of Fig. 2 is an example) in a L^3 box with 256^3 mesh points, so that the cell size was 1.04 Mm. As the filament is not located at the disk center, the projection effects are taken into account (see Démoulin et al. 1997). Moreover, the observed line-of-sight component of the magnetic field B_l is set to be the component perpendicular to the photosphere B_z .

The computation of the dips is performed only around the portion of the neutral line (NL) above which the filament was indicated in Figure 1. This corresponds to ± 80 Mm along the NL and around the center of the magnetogram shown in Figure 2. In this region, the precise locations where $B_z = 0$ are found by converging numerically on these lines, at each height levels considered, and using a linear

interpolation between each mesh points. This allows computation of the dips every 500 km. Equation (8) is then solved in double precision. As we assume that each dip is filled by dense plasma to a height $d = 300$ km (see § 3.2), only this portion of the dipped field lines is plotted on the results. Note that in some cases, there are field lines that achieve a maximum height, d' , lower than d on one side of their dip. In such conditions, some of the plasma is expected to fall on one side of the dip in order to reach a pressure equilibrium, so that in its final state, the plasma will fill the dip only up to the height d' . In such cases, d is automatically replaced by d' .

5.2. The Model Prediction

Nine of the ten parameters of the model could be fixed with good confidence. Their values are reported in Table 1. The only parameter that could not be fixed is f , although its value was estimated to be between 2 and 4. For simplicity, the decision was made to build three models, with the integer values $f = 2, 3$, and 4.

The three-dimensional distribution of dips computed for $\alpha = 2.3 \times 10^{-2} \text{ Mm}^{-1}$ and for three different values of f is shown in the left-hand column of Figure 3. The three models clearly show a common large-scale pattern for the distribution of the magnetic dips. This shows that the result is robust to changes of the parameter f in the range of values estimated in § 4.3. All models basically show four main features:

1. a long ($\simeq 40$ Mm) extended barb in the northwest part of the filament;
2. a fragmented barb in the northeast part of the filament;
3. an interruption in the middle of the spine of the filament on the east side of this barb; and
4. a thick ($\simeq 15$ Mm) and arrowhead-shaped (pointing toward the east) western extremity of the spine.

However, some small differences exist on small scales between the three models: $f = 3$ and 4 lead to a nearly straight and continuous spine around which the distribution of lateral dips is slightly dispersed, while $f = 2$ gives a distorted and interrupted spine with many lateral dips which look like continuous barbs. These minor differences are caused by the fact that a very large value of f implies that the imposed twisted flux rope dominates all the other fields, so it will have very small and very low lateral dips above the parasitic polarities. In contrast, a small value of f leads to a weak flux rope for which all the parasitic polarities can alter its coherent structure (in the extreme case $f = 0$, the flux rope will disappear and only dipped structures above parasitic polarities remain).

The model then predicts that the global morphology of the filament observed in H α should be close to what is obtained with the three models, and that one particular model may fit observed finer structures.

TABLE 1
FIXED VALUES FOR MODEL FREE PARAMETERS

$\tilde{B}(1;0)$ (G)	$\tilde{B}(2;0)$ (G)	$\tilde{B}(3;0)$ (G)	L (Mm)	δL (Mm)	$ \alpha /\alpha(\text{res})$	d (km)	a	H (Mm)
f	$-0.83 f$	$0.71 f$	266	$0.6 L$	0.99	300	1	10

NOTE.—See text for a description of the fixed values for the free parameters of the model. The only remaining parameters that can be varied are f (the flux of the bipolar background, which ensures the presence of a twisted flux rope for high $|\alpha|$) and the sign of α (giving the sign of helicity).

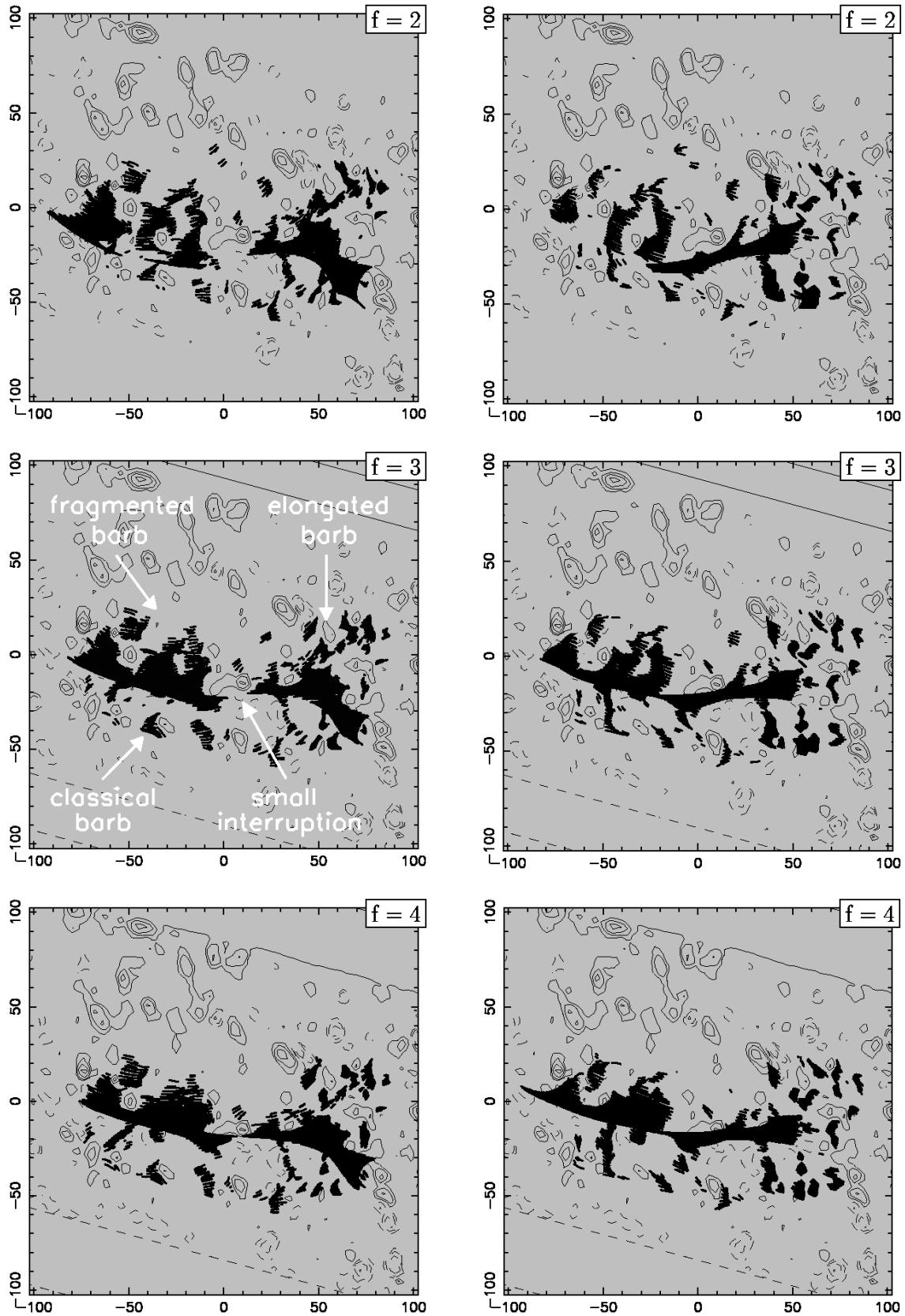


FIG. 3.—Linear magneto-hydrostatic reconstructions of a filament channel (observed on 1999/11/04 at E34S17) under the assumptions of the Aulanier et al. 1999 model. The NSO/KP magnetogram was taken at 17:31 UT. The left-hand panels indicate $\alpha > 0$; the right-hand panels indicate $\alpha < 0$. The gray plane is the photosphere. The solid (*dashed*) lines are isocontours of positive (*negative*) vertical field ($\pm 10, 20, 40$ G). The dark lines are magnetic dips drawn with a depth $d = 300$ km. They have been computed only at the places where the filament location was indicated (see Fig. 1).

5.3. Comparison with the H α Observation

It is only at this stage of our study that the H α image was compared with the models. We remind the reader of all the limitations of the modeling procedure, in particular, those concerning the uncertainties for the choice of some of the free parameters, but also considering that there is 1.5 hr time gap between the BBSO H α observation and the NSO/KP magnetogram, and adding to these all the limitations of the model listed in the Appendix B of Aulanier et al. (1999).

Despite these limitations, the models made a surprisingly good prediction for the global shape of the H α filament. The morphology of the spine as well as the location and the shape of the barbs is fairly well reproduced. Even though the three models give similar results on a large scale, overlays of the three-dimensional distribution of dipoles with the H α data reveal that $f = 3$ and 4 show a better agreement with the H α observation. Several features pointed out by arrows in Figure 1b are also identified on the models for which $\alpha > 0$ (see Fig. 3) and were predicted in § 5.2. The only observed structure that is poorly predicted is the “classical” barb on the southeast part of the filament, even though an isolated group of dipoles is present near its location.

One major feedback from this work is the possibility to interpret the four observed features that were successfully predicted. Using the same notations as in § 5.2, their respective interpretations are:

1. The long barb is formed by several disconnected groups of dipoles, which are associated with a discontinuous distribution of weak parasitic polarities with $B \leq 10$ G. The nearly continuous shape of this barb is caused by the distribution of these polarities along one very weakly curved line that extends away from the spine. The local topology of the field around each of these polarities is the same as the one shown in Figures 2a, 2b, 2d, 2e, and 6a and 6b in Aulanier et al. (1998).

2. The fragmented barb is formed in the same conditions as the elongated one, except that the associated polarities are fewer, slightly larger, and have mean fields of $B \simeq 15$ G.

3. The interruption in the spine is caused by a local intrusion in the neutral line (NL) by a strong positive polarity that has a peak value of $B \simeq 40$ G. This polarity locally alters the flux rope topology, leading to simply sheared arcades with no dip. This configuration is very similar to the theoretical result displayed in Figures 2c, 2f, and 6c in Aulanier et al. (1998).

4. The shape of the western end of the spine is caused by a local deformation of the twisted flux rope by two positive polarities which locally bend the NL toward the south. They have a peak of $B \simeq 40$ G. As the filament is far from disk center, the view in projection emphasizes this effect and leads to an apparent large thickness of the spine.

In these models, each lateral dip in the barbs is related to some observed weak photospheric parasitic polarity. This result is not new, as it has been shown already for purely theoretical configurations (Aulanier & Démoulin 1998; Aulanier et al. 1998; MacKay et al. 1999), as well as for models of observed filaments (Aulanier et al. [1998], [1999] studied one intermediate filament at four different times, and A. A. van Ballegoijen et al. [2000, in preparation] studied one active-region filament). All these studies combined with the observational results of Martin et al. (1994)

provide very strong arguments in favor of the association of the barbs with parasitic polarities.

6. PREDICTING THE SIGN OF HELICITY IN FILAMENT CHANNELS

In this section, we describe the results of extrapolations of the filament channel but now with negative helicity. We show that this model does not reproduce the observations as effectively. We also discuss what the model suggests for the origin of the chirality of the filament. Finally, we discuss how the model can be used to find the chirality and helicity of a filament.

6.1. Calculations with Opposite Helicity

As described in § 4.4, extending the results of Seehafer (1990), Pevtsov et al. (1995), and Canfield & Pevtsov (1998) for active regions to filaments, $\alpha > 0$ was chosen for the test model. The model produced a sinistral filament: the magnetic field pointed to the left along the filament axis and the barbs slant to the left from the filament axis to their chromospheric footpoint when viewed from the positive polarity (in accordance with the definition of Martin et al. 1994). This is because the modeled twisted flux rope (which forms the spine) had a right-handed twist (as in Low & Hundhausen 1995 and van Ballegoijen 1999). The structure of the observed spine and barbs was fairly well predicted by the variations of the model (see § 5.3). As in the H α observation, all the modeled barbs were not clearly right- or left-bearing, and, in particular, the southeast classical barb appeared to be right-bearing.

As a new test of the model, the same extrapolations as in § 4 are recalculated but this time for $\alpha = -2.3 \times 10^{-2} \text{ Mm}^{-1} < 0$. This leads to a dextral field orientation in the filament channel created by a left-handed twisted flux rope. The models are displayed in the right-hand column of Figure 3. At first sight, one can immediately notice that there are similarities with the $\alpha > 0$ case, in particular, the fragmented barb is also present. However, there are also many noticeable differences. The elongated barb is distorted and very fragmented. There are also several thin barbs that appear on the northern side of the spine, and the southeast classical barb is longer and thinner. In addition, the spine is also different, especially near the location of the interruption and the morphology of its western end.

We conclude that the model for the filament with $\alpha < 0$ gives significantly different results and also does not match the observations as well as those for which $\alpha > 0$. This second test confirms that the chirality of the filament is the same as the chirality of the majority of filaments in the southern hemisphere, which is sinistral. Under the assumptions of the model, sinistral filaments have the same helicity as the dominant helicity of active regions in the southern hemisphere. This assigns positive helicity to the filament.

6.2. On the Origin of the Orientation of Filament Barbs

The reason why some lateral dipoles (i.e., barbs) appear at the same locations for both signs of α is because their presence is strongly (but not only) constrained by the flux, the location, and the distribution of the parasitic polarities, which is given as boundary conditions by the magnetogram. Consequently, even if changing the sign of α strongly modifies the geometry of the field lines in the filament channel, some barbs are present in both cases. However, α

has a much more important effect on the larger fields. That is why on a large scale the modeled barbs do not have the same structure in both cases and why there are different interruptions in the spine of the filament.

We then get the interesting result that the orientation of filament barbs (i.e., right- or left-bearing) is not only constrained by the sign of the magnetic helicity (as proposed by Martin et al. 1994) but also by the distribution of the parasitic polarities. Aulanier & Démoulin (1998), Aulanier et al. (1998), and MacKay et al. (1999) have found that if a barb is related to one parasitic polarity only, it always follows the general chirality patterns proposed by Martin et al. (1994). However, for the filament modeled in the present study, most of the barbs are related to many small parasitic polarities, which is common for a large filament channel located in the quiet Sun. From the model point of view, the random distribution of these polarities (often along the edges of supergranules) is then very likely to produce complex patterns for the magnetic dips for the barbs. This is thought to be one of the reasons why some barbs of this filament have variability in their orientations.

The chirality of many large quiescent and/or polar crown filaments is very hard to determine when only the structure and orientation of the barbs is used (Zirker, Leroy, & Gaizauskas 1998). On the other hand, the chirality of intermediate and active-region filaments are more readily recognized (Martin 1998). This could be because, as intermediate as well as active-region filaments are usually located in narrower channels, fewer (or even only one) parasitic polarities are expected to be responsible for the presence of each barb.

6.3. *A New Tool for Determining the Chirality*

As discussed above, the sign of chirality in filaments and filament channels is sometimes difficult to infer only from their morphology. New models of the formation of filament channels in switchbacks (i.e., large-scale neutral lines having a horseshoe shape) show that, under some conditions, the axial fields may have opposite chiralities on the two sides of a switchback (van Ballegoijen, Cartledge, & Priest 1998; van Ballegoijen, Priest, & Mackay 2000). Both of these aspects clearly show a need for finding a method that ensures unbiased determination of the sign of chirality in filaments.

The results of our test, for which the calculations were done with opposite helicities while keeping all the free parameters of the model unchanged, show that the Aulanier et al. (1999) model can be used efficiently for this purpose.

7. CONCLUSION

This paper reports on the first attempt of prediction of the structure of one observed filament using a three-dimensional magnetic model developed by Aulanier et al. (1999). Only a single full-disk NSO/KP line-of-sight magnetogram was provided for the modeling, with the location of the filament axis (i.e., large-scale neutral line) indicated by a straight line. The BBSO H α image of the filament was revealed only after the modeling was done.

The model is based on linear magnetohydrostatic extrapolations. It includes a simplified form for the effects of plasma pressure and of gravity. The spine of the filament is assumed to be formed by a weakly twisted flux rope. The structure of the absorbing material observed in H α is assumed to be caused by the presence of overdensities

trapped in dipped portions of upward curved magnetic field lines. The model proposes that not only the filament spine, but also its barbs, are formed by magnetic dips. The dips in the spine are formed by the twisted flux rope, while those in the barbs are formed by the perturbation of the flux rope and of the surrounding sheared arcades by photospheric parasitic polarities. This theoretical association of the barbs with the parasitic polarities confirms the observational results of Martin (1990) and Martin et al. (1994).

The model depends on 10 free parameters; nine of them were fixed, and one (f) was varied in reasonable ranges. Based on the hemispheric helicity patterns for active regions found by Seehafer (1990), Pevtsov et al. (1995), and Canfield & Pevtsov (1998), a positive value for the force-free field parameter α was chosen. Then, using the NSO/KP magnetogram as boundary condition, the magnetic field above the filament channel was reconstructed. Subsequent comparison showed that the morphology of the filament predicted by the model was in a surprisingly good agreement with the shape of the observed H α filament.

The results show that the procedure described in this paper for the determination of the values of the parameters of the model is robust. Also, the model appears to be a powerful tool that can be used for prediction of the morphology of filament spines and barbs. However, the robustness of the method needs to be further tested through predictions of other observed filaments. Recently, van Ballegoijen, Priest, & Mackay (2000) proposed a model to predict the evolution of the spine of filaments. The combination of both approaches can be used for prediction of the evolution of filaments and their barbs.

Based on our model, we suggested that the orientation of the barbs is constrained not only by the sign of helicity, as proposed by Martin et al. (1994), but also by the distribution of the parasitic polarities in the filament channel. This explains why the filament we studied here had a right-bearing barb while the chirality of its field was sinistral. We then proposed an explanation to the difficulty of finding the chirality of quiescent and polar crown filaments (Zirker, Leroy, & Gaizauskas 1997).

As a second test, we repeated all the calculations, keeping the same values for all the free parameters, but we changed the sign of helicity. In that case, the modeled filament did not match the observations well.

This test for a single quiescent filament suggests that the method can be used to find the chirality and the magnetic helicity of other observed filaments, including those for which the chirality is not clear from the H α observations alone.

Part of this work was done during the PROM workshop, hosted by T. G. Forbes in University of New Hampshire on 1999 November 12–14. The authors thank all the participants of the workshop for witnessing the first comparison of the model predictions with the observations, as well as for their stimulating discussions. We also thank the Kitt Peak and Big Bear observatories for providing on-line magnetogram and H α data on the World Wide Web. We thank P. Démoulin, S. K. Antiochos, and the anonymous referee for helpful suggestions regarding the improvement of the manuscript. The work of G. A. is funded by NASA and ONR. The work of N. S. is funded by Max-Planck-Institut für Aeronomie. The work of S. F. M. is funded by NSF through grant ATM-9808063.

REFERENCES

- Alissandrakis, C. E. 1981, *A&A*, 100, 197
- Amari, T., & Aly, J.-J. 1992, *A&A*, 265, 791
- Amari, T., Luciani, J.-F., Mikić, Z., & Linker, J. 1999, *ApJ*, 518, L57
- Antiochos, S. K., Dahlburg, R. B., & Klimchuk, J. A. 1994, *ApJ*, 420, L41
- Antiochos, S. K., & Klimchuk, J. A. 1991, *ApJ*, 378, 372
- Antiochos, S. K., MacNeice, P. J., Spicer, D. S., & Klimchuk, J. A. 1999, *ApJ*, 512, 985
- Aulanier, G., & Démoulin, P. 1998, *A&A*, 329, 1125
- Aulanier, G., Démoulin, P., Mein, N., van Driel-Gesztelyi, L., Mein, P., & Schmieder, B. 1999, *A&A*, 342, 867
- Aulanier, G., Démoulin, P., van Driel-Gesztelyi, L., Mein, P., & DeForest, C. 1998, *A&A*, 335, 309
- Athay, R. G. 1990, *Sol. Phys.*, 126, 135
- Bommier V. 1998, in *ASP Conf. Proc. 150 (IAU Colloq. 167)*, New Perspectives on Solar Prominences, ed. D. Webb, B. Schmieder, & D. Rust (San Francisco: ASP), 434
- Canfield, R. C., & Pevtsov, A. A. 1998, in *ASP Conf. Proc. 140*, 18th NSO Sacramento Peak Summer Workshop, ed. K. S. Balasubramaniam, J. Harvey, & D. Rabin (San Francisco: ASP), 131
- Cheng, C. Z., & Choe, G. S. 1998, *ApJ*, 505, 376
- Dahlburg, R. B., Antiochos, S. K., & Klimchuk, J. A. 1998, *ApJ*, 495, 485
- Démoulin, P. 1998, in *ASP Conf. Proc. 150 (IAU Colloq. 167)*, New Perspectives on Solar Prominences, ed. D. Webb, B. Schmieder, & D. Rust (San Francisco: ASP), 386
- Démoulin, P., Bagalá, L. G., Mandrini, C. H., Hénoux, J.-C., & Rovira, M. G. 1997, *A&A*, 325, 305
- Démoulin, P., & Priest, E. R. 1989, *A&A*, 214, 360
- . 1992, *A&A*, 258, 535
- . 1993, *Sol. Phys.*, 144, 283
- DeVore, C. R., & Antiochos, S. K. 2000, *ApJ*, 539, 954
- Engvold, O. 1998, in *ASP Conf. Proc. 150 (IAU Colloq. 167)*, New Perspectives on Solar Prominences, ed. D. Webb, B. Schmieder, & D. Rust (San Francisco: ASP), 23
- Fieldler, R. A. S., & Hood, A. W. 1993, *Sol. Phys.*, 146, 297
- Filippov, B. P. 1995, *A&A*, 303, 242
- Forbes, T. G. 1997, in *Theoretical and Observational Problems Related to Solar Eclipses*, ed. Z. Mouradian & M. Stavinschi (Dordrecht: Kluwer), 149
- Galsgaard, K., & Longbottom, A. 1999, *ApJ*, 510, 444
- Gary, G. A., & Hagyard, M. J. 1990, *Sol. Phys.*, 126, 21
- Inhester, B., Birn, J., & Hesse, M. 1992, *Sol. Phys.*, 138, 257
- Jenssen, E. 1990, in *IAU Colloq. 117*, Dynamics of Quiescent Prominence, ed. V. Ruzdjak & E. Tandberg-Hanssen (New York: Springer), 129
- Kippenhahn, R., & Schlüter, A. 1957, *Z. Astrophys.*, 43, 36
- Kucera, T. A., Aulanier, G., Schmieder, B., Mein, N., & Vial, J. C. 1999, *Sol. Phys.*, 186, 259
- Kuperus, M., & Raadu, M. A. 1974, *A&A*, 31, 189
- Litvinenko, Y., & Martin, S. F. 1999, *Sol. Phys.*, 190, 45
- Low, B. C. 1992, *ApJ*, 399, 300
- . 1994, *Plasma Phys.*, 1, 1684
- Low, B. C., & Hundhausen, J. R. 1995, *ApJ*, 443, 818
- MacKay, D. H., Longbottom, A., & Priest, E. R. 1999, *Sol. Phys.*, 185, 87
- Malherbe, J.-M., & Priest, E. R. 1983, *A&A*, 123, 80
- Malherbe, J.-M., Schmieder, B., Ribes, E., & Mein, P. 1983, *A&A*, 119, 197
- Martin, S. F. 1990, in *IAU Colloq. 117*, Dynamics of Quiescent Prominence, ed. V. Ruzdjak & E. Tandberg-Hanssen (New York: Springer), 1
- . 1992, in *IAU Colloq. 133*, Eruptive Solar Flares, ed. Z. Svestka, B. Jackson, & M. Machado (New York: Springer), 330
- . 1998, *Sol. Phys.*, 182, 107
- Martin, S. F., Bilimoria, R., & Tracadas, P. W. 1994, *Solar Surface Magnetism (Dordrecht: Kluwer)*, 303
- Martin, S. F., & McAllister, A. H. 1997, in *Coronal Mass Ejections*, ed. N. Crooker, J. A. Joselyn, & J. Feynman (Washington, DC: AGU), 127
- Pevtsov, A. A., Canfield, R. C., & Metcalf, T. R. 1995, *ApJ*, 440, L109
- Priest, E. R. 1998, in *ASP Conf. Proc. 150 (IAU Colloq. 167)*, New Perspectives on Solar Prominences, ed. D. Webb, B. Schmieder, & D. Rust (San Francisco: ASP), 453
- Priest, E. R., Hood, A. W., & Anzer, U. 1989, *ApJ*, 344, 1010
- Rust, D. M., & Kumar, A. 1994, *Sol. Phys.*, 155, 69
- Schmieder, B. 1990, in *IAU Colloq. 117*, Dynamics of Quiescent Prominence, ed. V. Ruzdjak & E. Tandberg-Hanssen (New York: Springer), 85
- Schmieder, B., Démoulin, P., Aulanier, G., & Golub, L. 1996, *ApJ*, 467, 881
- Schmieder, B., Raadu, M. A., & Wiik, J. E. 1991, *A&A*, 252, 353
- Seehafer, N. 1990, *Sol. Phys.*, 125, 219
- Tandberg-Hanssen E. 1998, in *ASP Conf. Proc. 150 (IAU Colloq. 167)*, New Perspectives on Solar Prominences, ed. D. Webb, B. Schmieder, & D. Rust (San Francisco: ASP), 11
- Uchida, Y. 1981, *Proc. Japan-France Seminar on Sol. Phys.*, ed. F. Moriyama & J.-C. Hénoux, 169
- . 1998, in *ASP Conf. Proc. 150 (IAU Colloq. 167)*, New Perspectives on Solar Prominences, ed. D. Webb, B. Schmieder, & D. Rust (San Francisco: ASP), 384
- van Ballegooijen, A. A. 1999, *Magnetic Helicity in Space and Laboratory Plasma*, ed. M. R. Brown, R. C. Canfield, & A. A. Pevtsov (Washington, DC: AGU), 213
- van Ballegooijen, A. A., Cartledge, N. P., & Priest E. R. 1998, *ApJ*, 501, 866
- van Ballegooijen, A. A., & Martens, P. C. H. 1989, *ApJ*, 343, 971
- van Ballegooijen, A. A., Priest, E. R., & MacKay, D. H. 2000, *ApJ*, 539, 983
- Wang Y.-M. 1999, *ApJ*, 520, L71
- Wu, S. T., Bao, J. J., An, C. H., & Tandberg-Hanssen, E. 1990, *Sol. Phys.*, 125, 277
- Zirker, J. B., Leroy, J.-L., & Gaizauaskas, V. 1998, in *ASP Conf. Proc. 150 (IAU Colloq. 167)*, New Perspectives on Solar Prominences, ed. D. Webb, B. Schmieder, & D. Rust (San Francisco: ASP), 439
- Zirker, J. B., Martin, S. F., & Engvold, O. 1998, *Nature*, 396, 440